JOURNAL OF GUIDANCE, CONTROL, AND DYNAMICS
Vol. 22, No. 2, March–April 1999

Comparison of μ- and $\mathcal{H}_2$-Synthesis Controllers on an Experimental Typical Section

Jeffrey S. Vipperman[*]
University of Maine, Orono, Maine 04469-5711
Jeffrey M. Barker[†]
University of Minnesota, Minneapolis, Minnesota 55455
Robert L. Clark[‡]
Duke University, Durham, North Carolina 27708-0300
and
Gary J. Balas[§]
University of Minnesota, Minneapolis, Minnesota 55455

An experimental comparison of $\mathcal{H}_2$- and μ-synthesized flutter suppression control systems was performed. A simple parametric uncertainty can be used to track changes in system dynamics as a function of dynamic pressure. The control system was implemented experimentally on a NACA 0012 test model of a typical section mounted in a low-speed wind tunnel. The pitching angle, flap angle, and plunge deflection of the airfoil were measured with sensors and fed back through the control compensator to generate a single control signal commanding the trailing-edge flap of the airfoil. The model of the aeroelastic system, including the dynamics of the sensors and actuators in the bandwidth of interest, was obtained using system identification techniques. For comparison purposes, an $\mathcal{H}_2$ control system with standard linear quadratic Gaussian weightings also was designed and implemented. When compared to the $\mathcal{H}_2$ control system, the μ-synthesis controller provided better disturbance rejection in the bandwidth of the unsteady aeroelastic dynamics. In addition, the μ controller required less control energy than the $\mathcal{H}_2$ control system. The final advantage of μ-synthesis is the ability to design an aggressive μ control system that is stabilizing across the range of operating dynamic pressures.

Nomenclature

A, B, C, D = state-space representation of a system
F_u, F_l = upper and lower linear fractional transformations (LFT), respectively
I = identity matrix
J = cost functional
K = controller
L_i = input return difference matrix, $(I + KP)$
L_o = output return difference matrix, $(I + PK)$
P = generalized plant
Q, R = performance and control penalties, respectively, for linear quadratic Gaussian (LQG) design
u = control signal
V, W = process and sensor noise matrices, respectively, for LQG design
V_f = flutter speed
$\boldsymbol{w}$ = disturbance input to generalized plant
$\boldsymbol{w}_d, \boldsymbol{w}_n$ = process and sensor noise, respectively, for LQG design
$\boldsymbol{y}$ = measured plant variables
z = output of generalized plant
Δ = uncertainty model
μ = structured singular value
$\sigma(\omega)$ = plot of singular values vs frequency
ω = natural circular frequency

Subscripts

act = actuator
add = additive
par = parametric
perf = performance

Symbols

$\|\cdot\|_2$ = two norm
$\|\cdot\|_\infty$ = infinity norm

Introduction

FLUTTER is a dynamic instability, first characterized in detail by Theodorsen,[1] that can result in catastrophic mechanical failure of an aircraft wing. Because of the severity of the potential problem, aircraft today typically operate at conditions well below the flutter boundary. As aircraft design moves toward lighter-weight materials in efforts to improve fuel efficiency and aircraft agility, it is anticipated that aircraft will operate closer to the flutter boundary. Hence, active flutter suppression becomes increasingly important in ensuring the safety and efficiency of future aircraft.

The problem of active flutter suppression thus has received much attention, in the form of the active flexible wing (AFW) program[2–4] and the benchmark active controls technology (BACT) model, which was developed at NASA Langley Research Center specifically to address flutter and its suppression.[5–10] The AFW has been used for testing various single input/single output and multi-input/multi-output controllers. Digital implemention and wind-tunnel tests conducted at NASA Langley Research Center's 16-ft Transonic Dynamics Tunnel in both air and heavy gas indicate an increase in flutter boundary from approximately 150 psf to the tunnel limit of 200 psf for a classical control law.[11,12] The BACT model also has been used to develop some adaptive control schemes using predictive control.[13,14]

$\mathcal{H}_2$ control, $\mathcal{H}_\infty$ synthesis, and μ-analysis and μ-synthesis have been implemented successfully on a two-dimensional thin airfoil

---

Received March 19, 1998; revision received Oct. 4, 1998; accepted for publication Oct. 6, 1998.

[*] Assistant Professor, Department of Mechanical Engineering, 5711 Boardman Hall. Member AIAA.

[†] Graduate Research Assistant, Department of Aerospace Engineering and Mechanics, 107 Akerman Hall. Student Member AIAA.

[‡] Associate Professor, Department of Mechanical Engineering and Materials Science, Box 90300. Member AIAA.

[§] Associate Professor, Department of Aerospace Engineering and Mechanics, 107 Akerman Hall. Member AIAA.

flutter model[15,16] based on Theodorsen's classical formulation.[1] These papers demonstrate good performance about the nominal model with $\mathcal{H}_2$ control and mixed $\mathcal{H}_2-\mathcal{H}_\infty$ control, and increased stability margins with $\mathcal{H}_\infty$- and μ-synthesis techniques. The actuators used for aeroelastic control include flaps[4,17] and/or spoilers[2] as well as strain actuation.[18,19]

This paper experimentally demonstrates and contrasts the success of $\mathcal{H}_2$ control and μ-synthesis in active flutter suppression on a wind-tunnel model of a typical section airfoil with a trailing-edge flap that serves as the control input. The aeroelastic model of the airfoil, which includes the transducer dynamics, is determined using system identification techniques. In the μ-synthesis control design, a parametric uncertainty model was developed to account for the unsteady dynamics of the aeroelastic system as a function of dynamic pressure. In addition, an additive uncertainty model in the μ design accounts for unknown high-frequency dynamics and serves to limit the bandwidth of the controller primarily to the region of the unsteady dynamics.

The next section describes the experimental testbed, which consists of a typical section airfoil that is equipped with a flap actuator assembly and installed in a low-speed wind tunnel. Dynamic models of this system are obtained through experimental system identification. Detailed descriptions of the μ and $\mathcal{H}_2$ control-system designs follow, where fundamental differences between the two designs are highlighted. Of particular significance is the description of how the additive and parametric uncertainty models were developed for the μ-synthesis procedure. Finally, the results are presented, starting with analytical comparisons of the open- and closed-loop systems in frequency domain. The experimentally measured control results include both time- and frequency-domain responses.

System Description

This section describes the typical section airfoil design, low-speed wind tunnel, and test equipment which comprised the test bed for the closed-loop control experiments.

Wing Model

The experimental model is shown in Fig. 1. Approximately the same experimental setup as used for this study was well described in an earlier work.[17] The only difference was that the actuator assembly for the flap was redesigned as described in the next section. The rectangular wing was based on a NACA 0012 airfoil shape consisting of a main wing with a 19-cm chord and 52-cm span and a trailing-edge flap with a 6.35-cm chord and 52-cm span that rotates relative to the main wing about a pinned axis. The dimensions of the airfoil help to minimize end effects and maintain a two-dimensional flowfield. The main wing is constructed from an aluminum-alloy circular spar beam that serves as the pitch axis, located at the quarter-chord location from the leading edge. The flap is constructed in a similar manner with an aluminum-alloy tube spar beam passed through the leading edge. Rotational variable differential transformers (RVDTs) were mounted to the upper ends of the flap and wing rotational axes to measure the angular deflection of each airfoil independently. Similarly, an RVDT was mounted to ground and attached to the upper support platform for the wing via a stiff rod such that the plunge displacement of the wing was measured as rotation about the grounded RVDT. The cosine error of this measurement for typical displacements of 2 cm was less than 0.5%. The three RVDT signals serve as input signals to the control system as well as variables to categorize open-loop and closed-loop behavior of the typical section.

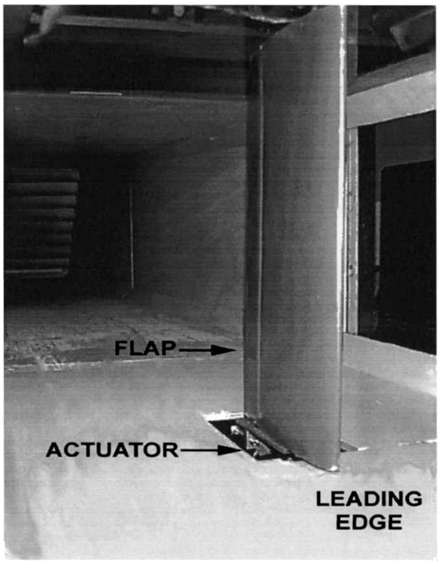

Fig. 1 Photograph of experimental model, as mounted in the Duke University Low-Speed Wind Tunnel.

Table 1 Measured modal properties of the typical section airfoil

Mode	Resonant frequency, Hz	Damping, %
Pitch	3.7	1.7
Plunge	7.0	2.6
Flap	15	17

As seen in Fig. 1, the model is mounted vertically in the wind tunnel. The support mechanisms for the model are mounted outside of the wind tunnel, at the top and bottom. Each support mechanism consists of a guided cantilever beam[20] made of two steel leaf springs that are 20.32 cm long, 2.86 cm wide, and 0.102 cm thick. The distance between the two leaf springs that make up each guided cantilever beam is 15.24 cm. A support block joins the free ends of the two leaf springs and these upper and lower support blocks translate with the model along the plunge degree of freedom. The pitch axis of the main wing is mounted to the upper and lower support blocks through a pair of precision bearings, which have a small amount of dry friction in the ball. At the upper bracket, there is a spring wire that is press-fitted through the center of the shaft and simply supported at each end to form the pitch stiffness. Supports at each end of the spring wire can be moved in or out to increase or decrease, respectively, the stiffness of the pitch axis. A similar spring was mounted to the bottom of the flap axis to provide the restoring stiffness. Table 1 shows the resonant frequencies and damping (viscous model) for the three modes of the typical section in the absence of aerodynamic forces. Detailed stiffness and inertial properties prior to the addition of the control actuator assembly for all three degrees of freedom (pitch, plunge, and flap) can be found in the literature.[21] These properties were chosen to give a flutter speed ($V_f = 18.8$ m/s) well below the maximum speed achievable by the wind tunnel.

The flap was chosen as the single control actuator to demonstrate the feasibility of active flutter suppression using an existing aeroelastic control surface. Sensors were attached to the typical section that will independently measure the three mechanical degrees of freedom: pitch angle, plunge displacement, and flap angle. Feeding back measurements of pitch and plunge to the control system are obvious choices because these two mechanical modes become coupled through the aeroelastic relations and coalesce in frequency at the flutter boundary, where one of the two modes will become unstable. The flap position measurement completes the information about the mechanical states and provides some additional check on control effort.

Control Actuator Assembly

A schematic of the experimental control assembly is shown in Fig. 2. A BEI Sensors and Systems Company linear actuator, LA13-12-000A, serves as the means of applying the required control force to the experimental model. The field assembly is held stationary in a support block that is mounted to a base plate used to support all of the control system hardware. Two precision linear bearings are mounted on the base plate and support a mating precision shaft that is threaded into the center of the coil assembly. The mass of the actuator assembly is 0.42 kg.

The position of the coil assembly is measured using a Lucas Schaevitz 250 MHR linear variable differential transformer (LVDT), shown in Fig. 2. The core of the LVDT is attached to the shaft, and the body of the LVDT is mounted in a support block. The output of the

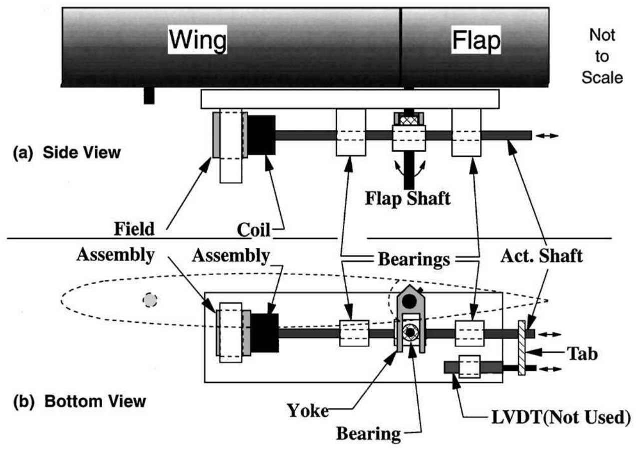

Fig. 2 Schematic diagram of experimental control assembly.

LVDT was not used for the control experiments, but rather allowed the output of the flap sensor to be corroborated through coherence measurements. The same transducers and spacing described in an earlier work[17] were used; however, the control actuator assembly was redesigned as follows: to decouple the actuator mechanism and restore stiffness. The linear motion of the BEI actuator is converted into the rotational motion of the flap using an aluminum yoke and bearing, as shown in Fig. 2. The yoke was attached to the flap shaft using a set screw and creates a 1.2-cm moment arm about the shaft. A precision bearing that fits between the arms of the yoke was mounted on a small aluminum block, which in turn was mounted to the actuator shaft using a set screw. As the BEI actuator shaft translates back and forth, the attached bearing forces the yoke to impart a torque to the flap shaft because it is rigidly attached with set screws. For a flap displacement of ±10 deg, the cosine error for the assembly is less than 1%, providing a negligible degree of nonlinearity. The entire control assembly is mounted to the lower end of the wing aileron. A cutout must be made in the floor of the tunnel to allow the actuator assembly to extend beyond the main wind-tunnel test section, as seen in the photograph of Fig. 1. Because the control actuator is mounted to the main wing, the entire assembly will pitch and plunge with the airfoil.

Wind Tunnel

All tests of the two-dimensional wing model were performed in the Duke University wind tunnel. The wind tunnel is a closed-circuit tunnel with a test section of 0.70 m × 0.51 m and a length of 1.22 m. The maximum attainable airspeed is 89 m/s. The stagnation temperature of the airstream is held constant over the range 15–38°C by means of an external air exchange system and tunnel stagnation pressure equals atmospheric pressure at the low-Reynolds-number operating conditions. For the present test, the Reynolds number based upon model chord is 0.52×10^6.

Signal Processing

Analog and digital signal processing hardware was required to implement the control systems. The μ and $\mathcal{H}_2$ control systems were discretized and implemented using a TMS320C40-based digital signal processor (DSP) board installed in a host personal computer. A mix of C and assembly languages were used to implement the discrete-time, state-space systems. Analog low-pass antialiasing filters as well as low-pass reconstruction filters were used on the input and output signals to the DSP, respectively. All times and frequency-domain signal analysis was performed using a six-channel, Siglab 20-22 spectrum analyzer. System identifications were accomplished by simultaneously curve fitting the measured frequency response functions (FRFs) for each of the three control path transfer functions, using SmartID[22] software. Note that, because the aeroelastic system models were determined through experimental system identification, unstable open-loop models above V_f were not available. The derived models contained 15 states and agreed very well with the measured FRFs. The measured system contains one electrical state, eight mechanical states (pitch, plunge, flap, actuator), aerodynamic states, and a slight degree of overdetermination typical in most system identifications. The $\mathcal{H}_2$ designs used the full 15-state model; however, for the μ-synthesis, the models were truncated to six states corresponding to the pitch, plunge, and flap degrees of freedom. The truncation greatly simplified the addition of a parametric uncertainty model.

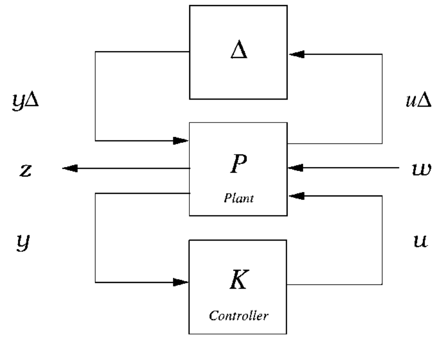

Fig. 3 General control design structure including model uncertainty.

Control System Designs

The basic structure for control system design is shown in Fig. 3, where the plant and compensator are represented by P and K, respectively; $\boldsymbol{w}(t)$ is a set of weighted exogenous inputs; $z(t)$ is a set of weighted exogenous outputs to be minimized; $y(t)$ are the measured plant outputs; and $u(t)$ is the control signal. Generalized lumped uncertainty is represented by the Δ block. The exogenous output $z(t)$ can be written in terms of a lower linear fractional transformation (LFT) of P and K, $F_l(P, K)$ as

$$z = F_l(P, K)\boldsymbol{w} = \left[P_{11} + P_{21}K(I - P_{22}K)^{-1}P_{21}\right] \tag{1}$$

where the plant is partitioned as

$$P = \begin{bmatrix} P_{11} & P_{12} \\ P_{21} & P_{22} \end{bmatrix} \tag{2}$$

such that the dimensions are consistent with $\boldsymbol{z}$, $\boldsymbol{y}$, $\boldsymbol{w}$, u, and K as shown in Fig. 3. A corresponding upper LFT, $F_u(P, K)$, is defined in an analogous manner. For disturbance rejection, it is desired to minimize the response of $z(t)$. The optimal compensators K that accomplish this task can be obtained by minimizing either $\|F_l(P, K)\|_2$ or $\|F_l(P, K)\|_\infty$, which corresponds to minimizing the $\mathcal{H}_2$ or $\mathcal{H}_\infty$ norms of $z(t)$, respectively.

Often with robust control designs, explicit robust stability (RS) or robust performance (RP) objectives are stated. For the purpose of this study, there were no such goals, but rather the loops were closed on the control designs and the new stability margins were determined experimentally by gradually increasing the flow rate until the onset of the closed-loop flutter boundary. Also, although the experimental system identification often can provide more accurate models of lightly damped structural systems, the technique suffers from the inability to obtain the unstable open-loop models above the flutter boundary. If desired, an experimentally obtained mechanical model could be combined with the analytical approximations of the aeroelastic states to combine the best of both modeling techniques.

μ-Synthesis

In this section a brief background on the structured singular value is provided along with a discussion of the D–K iteration technique. Consult Refs. 23–25 for a more detailed description of structured singular value (μ) analysis and synthesis theory.

Structured Singular Value (μ)

The structured singular value provides a framework for analyzing the stability and performance of uncertain systems. Figure 4 shows the general framework that will be used for system analysis. The outputs $z(t)$ can be represented in terms of an upper linear fractional transformation of M with Δ: $z = F_u(M, \Delta)w = [M_{22} + M_{21}\Delta(I - M_{11}\Delta)^{-1}M_{12}]$, where $M = F_l(P, K) = [P_{11} + P_{12}K(I - P_{22}K)^{-1}P_{21}]$.

The Δ block in LFT representation is defined as having a special structure, that is, $\Delta \in \boldsymbol{\Delta}$, where $\boldsymbol{\Delta}$ is a set of block diagonal matrices defined by

$$\boldsymbol{\Delta} = \left\{\mathrm{diag}\left(\delta_1^c I_{q1}, \ldots, \delta_n^c I_{q_n}, \Delta_1, \ldots, \Delta_F\right) : \delta_i^c \in C,\ \Delta_j \in C^{m_j \times m_j}\right\}$$

Definition: For $M \in C^{n \times n}$, $\mu_\Delta(M)$ is defined by

$$\mu_\Delta(M) = \frac{1}{\min\{\bar{\sigma}(\Delta) : \Delta \in \boldsymbol{\Delta}, \det(I - M\Delta) = 0\}}$$

and, if $(I - M\Delta)$ is not singular for any $\Delta \in \boldsymbol{\Delta}$, then $\mu_\Delta(M) = 0$. The structured singular value μ is a measure of the smallest destabilizing perturbation for a matrix. The structured singular value μ thus can be used to evaluate robustness margins for a linear system with structured uncertainty. The design guarantees the following stability properties stated as Theorems 1 and 2.

Theorem 1: $F_u(M, \Delta)$ is stable $\forall\, \Delta \in \boldsymbol{\Delta}$ iff $\sup_w \mu_\Delta(M_{11}\,(jw)) \leq 1,\ 0 \leq w \leq \infty$.

This theorem provides a test for the stability of the system shown in Fig. 4. If $\mu_\Delta(M_{11}(j\omega)) \leq 1$ for all allowable perturbations, the system achieves RS.

The RP problem can be formulated as an RS problem by associating a fictitious full block of uncertainty, Δ_{perf} with the performance inputs and outputs. Consider a new $\underline{\Delta}$ structure defined as

$$\underline{\Delta} = \left\{\begin{bmatrix} \Delta & 0 \\ 0 & \Delta_{\mathrm{perf}} \end{bmatrix} : \Delta \in \boldsymbol{\Delta},\ \Delta_{\mathrm{perf}} \in C^{n_w \times n_z}\right\} \tag{3}$$

An RP test then is given by the following theorem.

Theorem 2: $F_u(M, \Delta)$ is stable and $\|F_u(M, \Delta)\|_\infty < 1\ \forall\, \Delta \in \boldsymbol{\Delta}$ iff $\mu_{\underline{\Delta}}(M) < 1$.

Theorem 2 implies that performance robustness of a closed-loop system can be evaluated by a μ test across all frequencies. This gives an analysis test that can be used on the closed-loop system to check that the controller achieves the required stability and performance objectives. Proofs of the two theorems and variations can be found in the literature.[23–25]

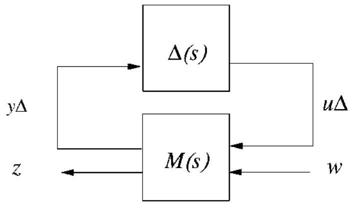

Fig. 4 LFT structure.

In designing a control algorithm for flutter control, two objectives are important. The first is to stabilize the system over a wide range of operating conditions, and the second is to attenuate disturbances throughout the operation envelope. As the preceding theorems show, the structured singular value μ provides a framework for evaluating a system's RS and RP properties. Therefore, finding a controller K that minimizes $\mu_{\underline{\Delta}}$ is a natural approach to satisfying RS and RP requirements. This approach is called μ-synthesis.

The D–K iteration control design technique is an approximation to μ-synthesis that has been used with significant success.[22] Although this approach does not guarantee that a global or even a local minimum will be reached, experience shows that the D–K iteration control design technique works well for many engineering problems.

μ-Design

The main objective for active control of the Duke flexible wing is to design a single controller for all operating points that also extends the flutter boundary. Meeting this objective requires improved performance (disturbance rejection) at velocities below the flutter boundary, stability and satisfactory performance at higher velocities, and limiting actuator response due to hard actuator constraints. Figure 5 shows a block diagram of the interconnection structure used for controller synthesis. The inputs to the controller are the pitch, plunge, and flap displacement measurements of the wing. The controller output is a deflection command to the flap actuator. The deflection limit of the actuator used for flutter control is ±2 V or ±10 deg.

The nominal plant model is taken at the 18.8-m/s operating point, the closest of the six linear models to the flutter boundary. For controller synthesis, the order of the nominal plant was reduced from a 15-state to a 6-state plant. The states in the reduced-order model correspond to the pitch and plunge modes of the wing, and one higher-frequency complex-conjugate pole pair. Additive and parametric uncertainty were used to account for uncertainty in the model and the range of operating conditions.

In the μ-synthesis framework, characterizing model uncertainty plays a large role in the success of the control design process. For the flutter problem, an additive uncertainty weight is used to account for model variations in the low-frequency gain and model uncertainty at higher frequencies, whereas parametric uncertainty accounts for the movement of the plunge pole pair from stable to unstable as velocity increases. These uncertainties are included so that the closed-loop system will meet the stability objectives, increasing the flutter boundary above its open-loop value while maintaining stability for lower velocities. The additive uncertainty weight on the single input channel is modeled as the first-order transfer function $W_{\mathrm{add1}} = [0.3(s + 10)]/(s + 100)$, as shown in Fig. 5. This uncertainty is scaled to an appropriate magnitude for each output channel

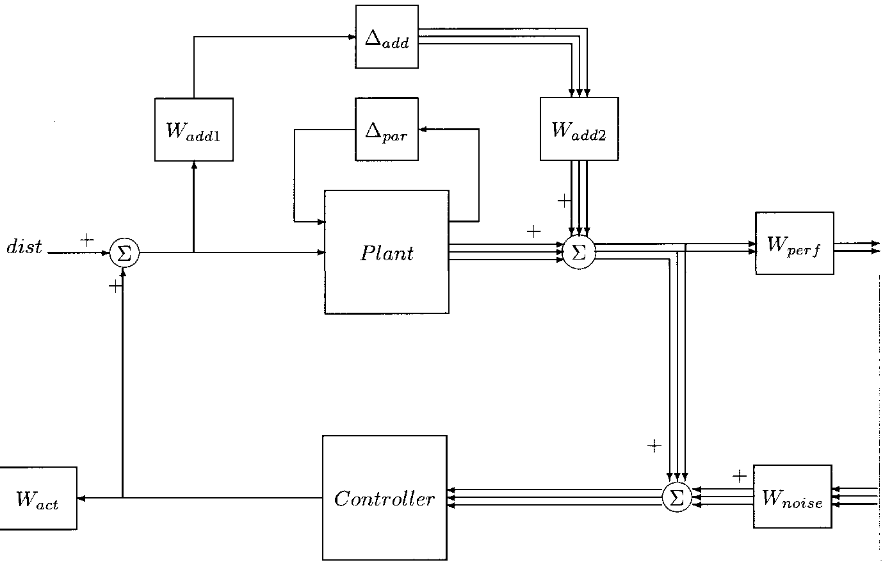

Fig. 5 Interconnection diagram for μ-design.

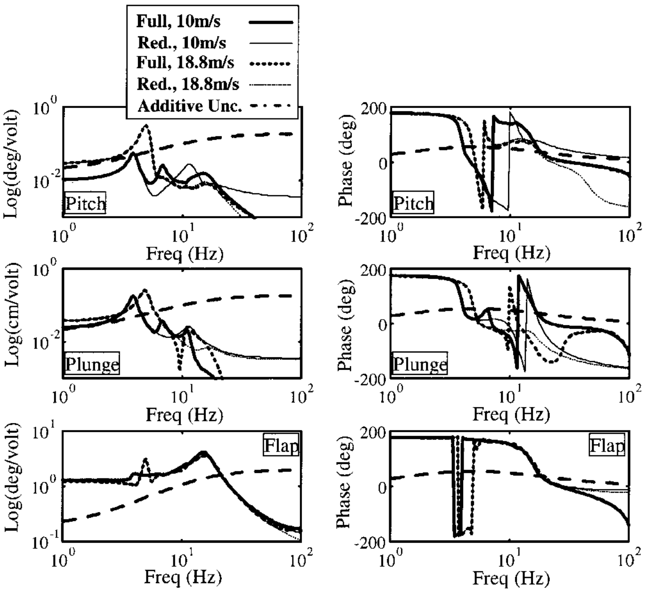

Fig. 6 Additive uncertainty (μ-design) and system model variation due to truncation for three open-loop channels.

through the constant scaling matrix $W_{\text{add2}} = \text{diag}[1, 1, \frac{4}{3}]$. This scaling allows a single transfer-function weight to be used to account for different uncertainty in three channels, thus keeping the number of states in the weighted plant small. Figure 6 shows the pitch, plunge, and flap transfer functions for the minimum (10 m/s) and maximum (18.8 m/s) velocities at which the wing was identified and the additive uncertainty in each channel. Recall that only the magnitude of the uncertainty weight is important. The weight encompasses all possible perturbing functions with magnitudes smaller than the additive weight. The level of the additive uncertainty at low frequencies (below 2 Hz) is selected so that the low-frequency magnitude of the nominal plant, plus or minus the magnitude of the uncertainty, includes all of the open-loop models. At high frequencies, the level of the uncertainty is selected to include the high-frequency dynamics and to induce the controller to roll off at those frequencies. The amount of additive uncertainty begins to increase just below the flutter frequency because, at this frequency, the differences in the nominal models become larger. Note that, in the 4 to 7-Hz region, additive uncertainty accounts for only part of the variation from the nominal model. Parametric uncertainty is added to the design model to account for the variation of the real part of a complex-conjugate pole pair at the flutter frequency (5 Hz). The parametric uncertainty was added to the first mode of the reduced system in order to model the instability that results at wind-tunnel velocities of just over 18.8 m/s. The A matrix of the reduced system is transformed to bidiagonal form and only the first element of the first block is treated as uncertain, resulting in a small change in natural frequency and a significant change in the damping level of the mode. Thus the migration of the pole pair toward the right half-plane as wind-tunnel velocity increases can be captured via parametric uncertainty. In this problem the varying parameter Δ_{par} is complex, thus introducing some additional conservativeness. This representation results in an unstable plant as the real part of Δ_{par} increases.

The performance objective is captured in the performance weighting $W_{\text{perf}} = \text{diag}[13, 8]$. These constant weights, applied to the pitch and plunge acceleration output channels, ask for a reduction of the maximum singular values from all inputs (disturbance on the actuator signal, uncertainty, and noise) to these outputs, thus decreasing the singular values by about an order of magnitude at the flutter frequencies. Meeting these performance weights would result in a significant increase in damping at the flutter frequency. For control design purposes, disturbances are introduced through an unweighted disturbance channel on the actuator command to the plant.

Also included in the problem setup are the constraint $W_{\text{act}} = 0.5$, to enforce the ±2 volt (±10 deg) actuator limits and the noise weight $W_{\text{noise}} = \text{diag}[0.0005, 0.001, 0.005]$ on the measurement signals. The actuator penalty function, W_{act}, penalizes actuator deflection to help ensure that the resulting controller will be relatively low gain. Each noise weight was chosen to be on the order of 1% of the magnitude of the dc gains of the actuator to pitch, plunge, and flap transfer functions. (Note that, if the uncertainty were modeled as input multiplicative, and the disturbance remained on the actuator input, then the noise channel would be necessary as the $\mathcal{H}_\infty$ design methodology requires that all measurements be corrupted.[23,24] In this problem, the additive uncertainty corrupts the measurements and the noise channel is not strictly necessary and in fact has little effect on the design).

$\mathcal{H}_2$ Control Design

For comparison purposes, an $\mathcal{H}_2$ control system using linear quadratic Gaussian (LQG) weightings was designed and implemented. LQG control systems have been successfully implemented for many classes of control problems, including active flutter control.[17] A plant model of the form

$$\dot{x} = Ax + Bu + w_d \tag{4}$$

$$y = Cx + w_n \tag{5}$$

where the process-noise w_d and sensor-noise w_n vectors, are Gaussian processes that satisfy $E[w_d(t)w_d(\tau)^T] = W\delta(t-\tau)$, $E[w_n(t)w_n(\tau)^T] = V\delta(t-\tau)$, $E[w_n(t)w_d(\tau)^T] = 0$, u is the single control input commanding the flap, and y are the three measured variables—pitch, plunge, and flap position. The LQG cost, which is of the form

$$J = E\left[\lim_{T\to\infty}\frac{1}{T}\int_0^T \left(x(t)^T Q x(t) + u(t)^T R u(t)\right)\mathrm{d}t\right] \tag{6}$$

where Q is a positive-semidefinite weighting matrix that determines the error or performance penalty and R is a positive-definite control penalty weighting matrix. Finding the optimal compensator K can be achieved by casting the LQG weighting scheme as an $\mathcal{H}_2$ minimization problem, $\min\{\|F_l(P, K)\|_2^2\}$, by constructing the generalized plant equation (2) in the following form:

$$P = \left[\begin{array}{ccc|c} A & W^{\frac{1}{2}} & 0 & B \\ Q^{\frac{1}{2}} & 0 & 0 & 0 \\ 0 & 0 & 0 & R^{\frac{1}{2}} \\ \hline C & 0 & V^{\frac{1}{2}} & 0 \end{array}\right] \tag{7}$$

Although frequency-domain weightings can be used in LQG designs to emphasize control in a particular interval and to limit the bandwidth of the control system, RS and RP cannot be satisfied simultaneously as in the μ-design. The LQG control design essentially contains an additive uncertainty model for the state derivatives (process noise) and sensor measurements (sensor noise), which are corrupted by Gaussian noises (w_d and w_n); this uncertainty model has been criticized as unrealistic for many classes of control problems. The process noise uniformly excites each state derivative of the aeroelastic system in an effort to provide some limited measure of RP. However, adding noise to the inputs of the plant states can result in instability. Additive noise in the sensor signals will serve to limit the bandwidth of the control system and compensate for unmodeled high-frequency dynamics at the expense of control performance in an effort to provide some measure of RS. Other shortcomings of LQG are a potentially unstable compensator, no guaranteed stability margins, and no explicit addressing of the pole uncertainty associated with the change in the aeroelastic system as a function of dynamic pressure as is possible with μ control designs that were outlined in the preceding section. Consequently, separate LQG controllers were designed for six different nominal operating points corresponding to 10-, 12.5-, 15.0-, 16.5-, 18.0-, and 18.8-m/s flow velocities, where the flutter boundary for the experimental typical section occurred at just above 18.8 m/s. Gain scheduling or another similar technique would be required to implement the series of LQG control systems in practice. Further, each LQG control system would not necessarily be stable at off-nominal flow speeds. However, the $\mathcal{H}_2$-designs used in this study were not overly aggressive and hence were stable at all flow speeds. Despite these potential shortcomings, good performance often can be achieved with an LQG compensator.

Controller Design

The linear μ controller was synthesized via the D–K iterative control design technique using the MATLAB μ-Analysis and Synthesis Toolbox.[22] The weighted open-loop system has seven states (the reduced six-state system plus one state for the additive uncertainty weight). After three iterations, a 23rd-order controller was obtained. A balanced realization of the controller was then obtained, and the 13 states with smallest singular value were truncated from the system. The resulting 10-state controller differs in $\mathcal{H}_\infty$ norm from the full-order controller by less than 1%.

Each LQG design was created using the Robust Control Toolbox in MATLAB. The parameters used in the definition of the generalized plant, Eq. (7), were $Q = \mathrm{diag}(1, 0.5)$, $R = 10^{-3}$, $W = I^{N\times N}$, $V = 10^{-3} \times I^{M\times M}$, where there are $N = 15$ states in the model and $M = 3$ sensor measurements. No iteration method was required because a closed-form solution to the $\mathcal{H}_2$ minimization problem exists.[24] The sensor noise V was decreased in decades from unity and then implemented on the real system to determine the lowest sensor noise level that can be used before an unstable closed-loop system results. Likewise, the control penalty R was decreased in the same manner in order to find the most aggressive control system possible that will result in a stable closed-loop system.

The performance of each control system is investigated analytically before being discretized using a Tustin transform and implemented on the experimental wind-tunnel model described earlier. The TMS320C40 DSP board easily supplied enough computational power to provide an ample sampling rate of 4 kHz.

Results

An analytical comparison of the open- and closed-loop responses using the models obtained from the system identification process reveals that both the $\mathcal{H}_2$ and μ control systems successfully reduce the plant response at the flutter frequency of approximately 5 Hz. Figure 7 displays these analytical results for four different flow speeds of 10, 15, 16.7, and 18.8 m/s. Note that a different $\mathcal{H}_2$ design was implemented for each flow speed. Figure 7 also shows significant attenuation of the magnitude peak associated with the first mechanical mode of the wing. In the 5-Hz region, the μ controller is predicted to attenuate disturbances better than the $\mathcal{H}_2$ design as a result of the parametric uncertainty model. Based on the simulation results, the μ controller is more successful in meeting the vibration attenuation performance goals.

Next, the discretized control systems were experimentally implemented on the wind-tunnel model. A measured increase of 8.5% (from 18.8 m/s to 20.4 m/s) was observed in the flutter boundary when the $\mathcal{H}_2$ control system was implemented on the wind-tunnel experiment. As expected, the μ control system increased the flutter boundary slightly further to greater than 20.7 m/s (10.1% increase in maximum velocity or a 21% increase in dynamic pressure, assuming incompressibility). Figures 8a–c show the identified open- and closed-loop magnitude plots for four system transfer functions at 16.7 m/s for both the $\mathcal{H}_2$ and the μ controllers. The pitch and plunge responses show that the μ controller notches out the primary flutter mode significantly, although it does not degrade performance at higher frequencies. The extent of the reduction in the first vibrational mode indicates that characterizing model variation with parametric uncertainty at the location of a pole pair is an effective design technique because the nominal control design model at 18.8 m/s had a different natural frequency and this is the 16.7-m/s model. The $\mathcal{H}_2$ controller also effectively reduces the flutter peak to dc magnitudes. The difference in the two control design methodologies is perhaps apparent as a result. The inclusion of parametric uncertainty in the μ-synthesis model framework gains additional performance at the critical frequency without sacrificing performance elsewhere. Comparing the experimental result in Fig. 8 with the simulated plunge magnitude plot (Fig. 7) serves to verify the accuracy of the identified open-loop models and the validity of the observations made while looking at the predicted closed-loop transfer functions. Finally, from the magnitudes of the measured frequency response functions of the control systems shown in Fig. 8d, it is seen that the μ control system requires less energy despite having better performance. The closed-loop control effort was particularly reduced for the μ design in the bandwidth of flutter instability around 5 Hz.

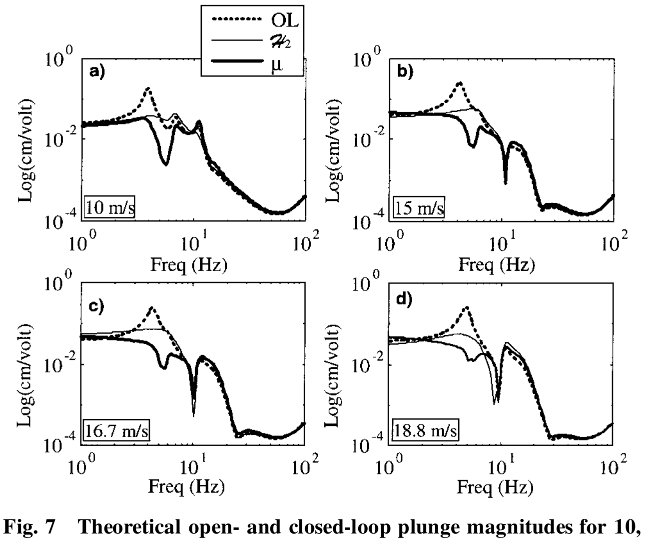

Fig. 7 Theoretical open- and closed-loop plunge magnitudes for 10, 15, 16.7, and 18.8 m/s.

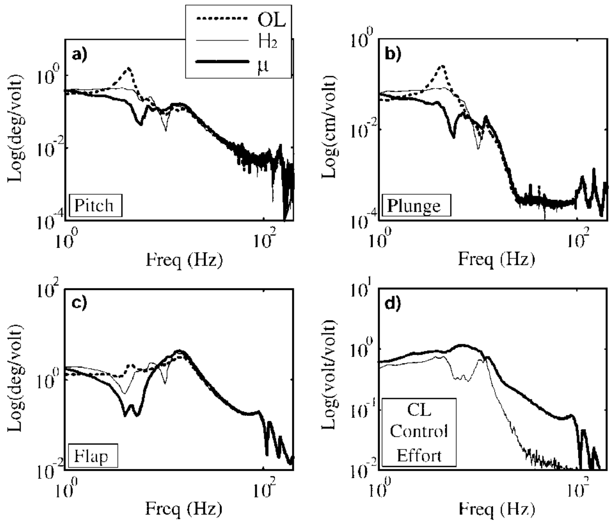

Fig. 8 Experimental open- and closed-loop transfer functions at 16.7 m/s (88% of V_f).

From Fig. 8, it can be observed that the μ control system, and to a lesser extent, the $\mathcal{H}_2$ control system significantly improves system performance in terms of disturbance attenuation throughout the operating range. This is significant because it shows that using active flutter suppression can reduce the magnitude of vibration at normal flight operating conditions, thus reducing the amount of strain placed on the wings. This indicates that less structural material may be needed for a wing using active aeroelastic control, and thus could lower the weight of the plane and the amount of fuel needed, resulting in less expensive flight.

Closed-loop frequency-domain results at flow rates above the open-loop flutter boundary V_f are presented in Fig. 9. The frequency-response magnitude is presented for each control case at the onset of closed-loop instability, which was determined experimentally to be 20.4 m/s for the $\mathcal{H}_2$ control system and 20.7 m/s for the μ control system. Note that the closed-loop response in the vicinity of the open-loop flutter frequency ($\approx$5 Hz) still exhibits good disturbance rejection from both control systems as indicated by the relatively low magnitudes in the closed-loop frequency responses. Resonant peaks at 12.25 Hz are observed in the plunge and closed-loop controller response in Fig. 9. This instability most likely is associated with the flap, which has an open-loop resonant frequency of 15 Hz.

Multivariable stability margins (MSMs), which characterize closed-loop-system stability robustness can be determined by considering additive plant uncertainties or by considering

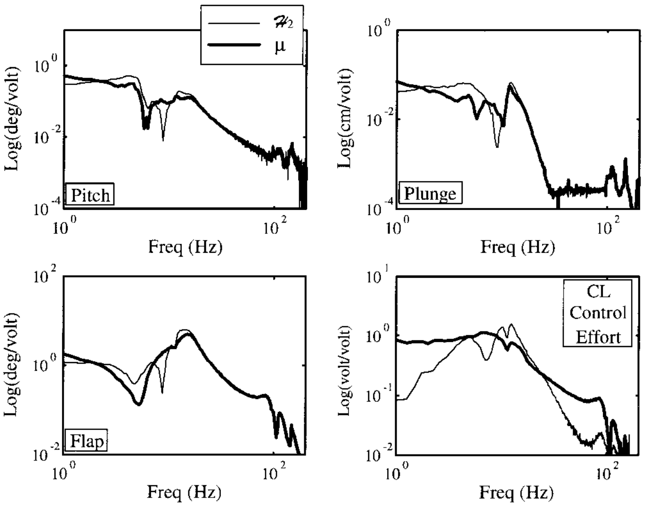

Fig. 9 Experimental closed-loop transfer functions at 20.4 m/s ($\mathcal{H}_2$) and 20.7 m/s (μ).

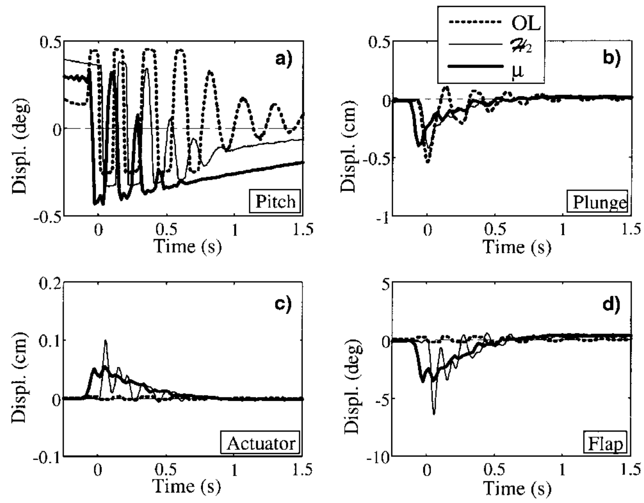

Fig. 11 Experimental time data for 16.7 m/s (88% of V_f).

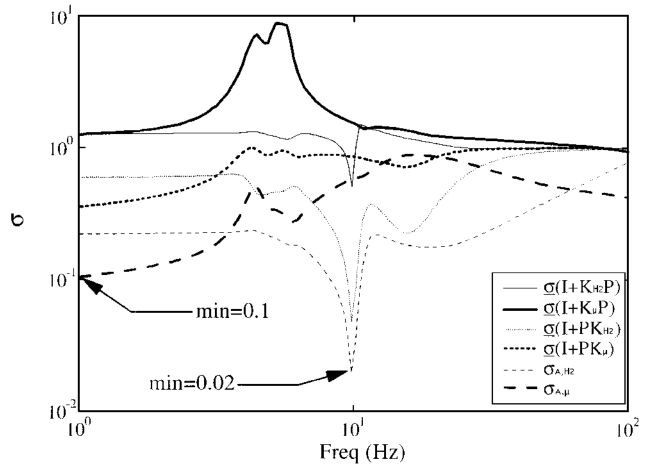

Fig. 10 Multivariable stability margins for $\mathcal{H}_2$ and μ controllers at 16.7 m/s (88% V_f).

multiplicative uncertainties on the plant input or outputs.[4,12] A multiplicative uncertainty on the plant input (output) can be investigated by plotting the minimum singular values of the plant input (output) return difference equations as a function of frequency or $\underline{\sigma}_{L_i}(\omega) = \sigma_{\min}[(I + KP)(\omega)]$ ($\underline{\sigma}_{L_o}(w) = \sigma_{\min}[(I + PK)(\omega)]$). Similarly, the RS with respect to an additive plant uncertainty can be determined from a plot of $\sigma_A = \sigma_{\max}\{[K(I + PK)^{-1}](\omega)\}^{-1}$. Figure 10 shows plots of these MSMs for the aeroelastic plant at a flow rate of 16.7 m/s for both the $\mathcal{H}_2$ and the μ controllers. Smaller minimum values of $\underline{\sigma}_{L_i}(\omega)$, $\underline{\sigma}_{L_o}(\omega)$, and $\sigma_A(\omega)$ indicated smaller stability margins for the respective type of uncertainty. The minimum values of $\underline{\sigma}_{L_i}(\omega)$, $\underline{\sigma}_{L_o}(\omega)$, and $\sigma_A(\omega)$ could be compared to the Universal gain and phase-margin diagram[26] in order to determine the relative phase and gain margins of the system at this particular flow rate. However, the stability margins depicted in Fig. 10 are very narrow and thus quantification is not necessary.

The light and heavy solid lines in Fig. 10 represent $\underline{\sigma}_{L_i,\mathcal{H}_2}(\omega)$ and $\underline{\sigma}_{L_i,\mu}(\omega)$ respectively. The minimum value of $\underline{\sigma}_{L_i,\mu}(\omega) = 0.93$ at 100 Hz and the minimum value of $\underline{\sigma}_{L_i,\mathcal{H}_2}(\omega) = 0.51$ at 9.8 Hz. Generally, these lines physically indicate that both controllers appear robust to uncertainties in the measurements of pitch, plunge, and flap angle that are fed back to the controllers. Next, plots of $\underline{\sigma}_{L_o,\mathcal{H}_2}(\omega)$ and $\underline{\sigma}_{L_o,\mu}(\omega)$ are given by light and heavy dotted lines in Fig. 10, respectively, and physically represent the sensitivity to uncertainty in the flap command. It can be seen that $\min(\underline{\sigma}_{L_o,\mathcal{H}_2}(\omega)) = 0.048$ at 9.8 Hz and $\min(\underline{\sigma}_{L_o,\mu}(\omega)) = 0.35$ at dc. The value of $\min(\underline{\sigma}_{L_o,\mathcal{H}_2}(\omega))$ is very low; however, it occurs past the critical frequency of 5 Hz. Finally, both control systems appear to be relatively sensitive to additive plant uncertainties as seen by the dashed lines in Fig. 10 ($\mathcal{H}_2$ in light dashed line and μ in heavy dashed line). The minimum values are seen to be $\min(\sigma_{A,\mathcal{H}_2}(\omega)) = 0.02$ at 9.8 Hz and $\min(\sigma_{A,\mu}(\omega)) = 0.1$ at dc. Overall, the μ controller is seen to have better stability robustness, which was observed experimentally. The bounds for the $\mathcal{H}_2$ system likely could be improved by incorporating a filter at 9.8 Hz that would increase the stability margins.

Figures 11a–d show the measured pitch, plunge, flap actuator position, and flap-angle time-response plots of the open-loop system and with the μ controller and $\mathcal{H}_2$ controller implemented. The plunge mode is the primary flutter mode, and both the μ and $\mathcal{H}_2$ controllers show a dramatic improvement over the uncontrolled system. This plot shows that active flutter suppression can be useful below the flutter boundary by effectively increasing the wing damping. They also achieve similar performance in the pitch mode. The $\mathcal{H}_2$ controller appears to have the quicker response, whereas the μ controller appears to provide greater energy dissipation. The quicker response of the $\mathcal{H}_2$ controller comes at the expense of increased actuator usage. The peak flap angle of the μ controller is about half that of the $\mathcal{H}_2$ controller for all of the wind-tunnel conditions tested. Additionally, the μ controller appears to use less control energy throughout the time simulation. This fits with the more conservative nature of μ-synthesis and indicates that the μ controller may stabilize the system for a larger class of disturbances.

Conclusions

Flutter suppression control system designs based on the structured singular value (μ) and $\mathcal{H}_2$ synthesis were implemented experimentally on a typical section airfoil and their performance was compared. Measurements of the three mechanical degrees of freedom for the typical section (plunge displacement, pitch angle, and flap angle) were measured and fed back to form a single control signal that commands the existing trailing-edge flap position. RS and RP were satisfied simultaneously within the μ-synthesis framework. The two design objectives were to increase the flutter boundary of the airfoil and to increase disturbance rejection below the flutter boundary of the system. The μ-synthesized control system was designed to be stable across flow speeds from one-half the open-loop flutter boundary up to the closed-loop flutter boundary, which is 10% higher than the open-loop flutter boundary. For comparison, an $\mathcal{H}_2$ control system based on LQG weightings was designed and implemented. Some level of RP and RS is provided by assuming that the state derivatives and sensor measurements are corrupted by uncorrelated Gaussian processes.

A successful μ-design and implementation relies upon intelligent choices for the system uncertainty models. The additive uncertainty used in this work was first-order high-pass in nature, where the low-frequency (<2 Hz) gain was chosen to encompass the differences between all three control paths and the high-frequency (>20 Hz) gain was chosen to limit the bandwidth of the controller such that unmodeled high-frequency dynamics are not destabilizing. The parametric uncertainty model characterizes the change in the poles of the aeroelastic system as a function of dynamic pressure within the range of design flow rates (10 m/s to $V_f = 18.8$ m/s). As such, μ-synthesis is well suited for the aeroelastic control problem, where the change in dynamics or uncertainty across the range of operating points is well understood.

Both the μ and $\mathcal{H}_2$ control designs were stable across the whole design interval $(0.5V_{fol} - V_{fcl})$. However, the μ controller provided significantly better disturbance rejection than the $\mathcal{H}_2$ controller, particularly in the interval of the aeroelastic pole migration (4–6 Hz) as a result of adding the parametric uncertainty model. The effort of the μ control system was primarily concentrated into this interval. In addition, the increase in the flutter boundary was higher for the μ controller than for the $\mathcal{H}_2$ controller (10.1% vs 8.5% increase), indicating better performance. Despite the better performance, the μ control system also uses less control energy than the $\mathcal{H}_2$ system in the example provided.

Acknowledgments

The authors gratefully acknowledge the U.S. Air Force Office of Scientific Research for funding this research under grant numbers F49620-96-1-0385, monitored by Major Brian Sanders, and F49620-95-1-0419, monitored by Marc Jacobs. Special thanks to Ran Cabell of NASA Langley Research Center for the TMS320C40 port of the control software.

References

[1] Theodorsen, T., "General Theory of Aerodynamic Instability and the Mechanism of Flutter," NACA 496, 1935.

[2] Waszak, M. R., and Srinathkumar, S., "Flutter Suppression for the Active Flexible Wing," *Journal of Aircraft*, Vol. 32, No. 1, 1995, pp. 61–67.

[3] Adams, W. M. J., and Christhilf, D. M., "Design and Multifunction Tests of a Frequency Domain-Based Active Flutter Suppression System," *Journal of Aircraft*, Vol. 32, No. 1, 1995, pp. 52–60.

[4] Mukhopadhyay, V., "Flutter Suppression Control Law Design and Testing for the Active Flexible Wing," *Journal of Aircraft*, Vol. 32, No. 1, 1995, pp. 45–51.

[5] Bennet, R., Eckstrom, C., Rivera, J. J., Dansberry, B., Farmer, M., and Durham, M., "The Benchmark Aeroelastic Models Program—Description and Highlights of Initial Results," NASA TM-104180, 1991.

[6] D'Cruz, J., "A Determination of the External Forces Required to Move the Benchmark Active Controls Testing Model in Pure Plunge and Pure Pitch," NASA TM-107743, 1993.

[7] Rivera, J. J., Dansberry, B., Bennet, R., Durham, M., and Silva, W., "NACA 0012 Benchmark Model Experimental Flutter Results with Unsteady Pressure Distributions," AIAA/ASME/ASCE/AHS/ASC Structures, Structural Dynamics, and Materials Conf., Dallas, TX, April 1992.

[8] Rivera, J. J., Dansberry, B., Farmer, M., Eckstrom, C., Seidel, D., and Bennet, R., "Experimental Flutter Boundaries with Unsteady Pressure Distributions for the NACA 0012 Benchmark Model," AIAA Paper 91-1010, April 1991.

[9] Scott, R., Hoadley, S., Wieseman, C., and Durham, M., "The Benchmark Active Controls Technology Model Aerodynamic Data," 35th AIAA Aerospace Sciences Meeting and Exhibit, Reno, NV, AIAA Paper 97-0829, Jan. 1997, p. 11.

[10] Waszak, M. R., "Modeling the Benchmark Active Control Technology Wind-Tunnel Model for Application to Flutter Suppression," *Proceedings of the AIAA Atmospheric Flight Mechanics Conference* (San Diego, CA), AIAA, Reston, VA, 1996.

[11] Adams, W. M., Chisthoff, D. M., Waszak, M. R., Mukhopadhyah, V., and Srinathkumar, S., "Design, Test, and Evaluation of Three Active Flutter Suppression Controllers," NASA TM-4338, 1992.

[12] Pototzky, A. S., Weiseman, C., Hoadley, S. T., and Mukhopadhyay, V., "On-Line Performance Evaluation of Multiloop Digital Control Systems," *Journals of Guidance, Control, and Dynamics*, Vol. 15, No. 4, 1992, pp. 878–883.

[13] Haley, P., and Soloway, D., "Generalized Predictive Control for Active Flutter Suppression," *IEEE Control Systems*, Vol. 17, No. 4, pp. 64–70.

[14] Lichtenwalner, P. F., Little, G. R., Pado, L. E., and Scott, R. C., "Adaptive Neural Control for Active Flutter Suppression," *Proceedings of the ASME Fluids Engineering Division*, Vol. 242, American Society of Mechanical Engineers, New York, 1996, pp. 3–8.

[15] Tokur, O., and Ozbay, H., "Robustness Analysis of Controllers Designed for Active Flutter Suppression," *Proceedings of the American Control Conference*, Vol. 1, 1995, pp. 182, 183.

[16] Ozbay, H., and Bachmann, G. R., "$\mathcal{H}_2/\mathcal{H}_\infty$ Controller Design for a Two-Dimensional Thin Airfoil Flutter Suppression," *Journal of Guidance, Control, and Dynamics*, Vol. 17, No. 4, 1994, pp. 722–728.

[17] Vipperman, J. S., Clark, R. L., Conner, M. D., and Dowell, E. H., "Experimental Active Control of a Typical Section Using a Trailing Edge Flap," *Journal of Aircraft*, Vol. 35, No. 2, 1998, pp. 224–229.

[18] Lazarus, K. B., and Crawley, E. F., "Multivariable Active Lifting Surface Control Using Strain Actuation: Analytical and Experimental Results," 3rd International Conf. on Adaptive Structures, San Diego, CA, Vol. 2040, 1993, pp. 87–101.

[19] Lin, C. Y., Crawley, E. F., and Heeg, J., "Open Loop and Preliminary Closed Loop Results of a Strain Actuated Active Aeroelastic Wing," *36th AIAA/ASME/ASCE/AHS/ASC Structures, Structural Dynamics, and Materials Conference* (New Orleans, LA), AIAA, Washington, DC, 1995, pp. 1904–1914.

[20] Roark, R. J., and Young, W. C., *Roark's Formulas for Stress and Strain*, McGraw–Hill, New York, 1989.

[21] Conner, M. D., Tang, D., Dowell, E. H., and Virgin, L. N., "Nonlinear Behavior of a Typical Airfoil Section with Control Surface Freeplay: A Numerical and Experimental Study," *Journal of Fluids and Structures*, Vol. 11, 1997, pp. 89–109.

[22] Active Control eXperts, Inc., *Smart ID System Identification Software*, Cambridge, MA, 1995.

[23] Balas, G., Doyle, J., Glover, K., Packard, A., and Smith, R., *μ-Analysis and Synthesis Toolbox*, MUSYN Inc. and MATHWORKS Inc., Minneapolis, MN, 1995.

[24] Zhou, K., Doyle, J., and Glover, K., *Robust and Optimal Control*, Prentice–Hall, Englewood Cliffs, NJ, 1996.

[25] Stein, G., and Doyle, J. C., "Beyond Singular Values and Loop Shapes," *Journal of Guidance, Control, and Dynamics*, Vol. 14, No. 1, 1991, pp. 5–16.

[26] Mukhopadhyay, V., Pototzky, A. S., and Fox, M. E., "A Scheme for Theoretical and Experimental Evaluation of Multivariable System Stability Robustness," *American Controls Conference*, American Automatic Control Council, Green Valley, AZ, 1990, pp. 3046, 3047.